Assessment of the Contribution of Polarimetric Persistent Scatterer Interferometry on Sentinel-1 Data

Jiayin Luo, Juan M. Lopez-Sanchez, *Senior Member, IEEE*, Francesco De Zan, Jordi J. Mallorqui, *Senior Member, IEEE*, and Roberto Tomás

***Abstract*—Time series of Sentinel-1 data are widely used for monitoring displacements of the Earth surface using persistent scatterer interferometry. By default over land, Sentinel-1 images include two polarimetric channels: 1) VV and 2) VH. However, most works in this application exploit only the VV channel, whereas the VH channel is discarded for its lower amplitude. Thanks to the development of polarimetric persistent scatterer interferometry methods, one can integrate multipolarization channels into a single optimal one. Previous studies proved that the number and spatial density of measurement points is increased. In this work, we explore the reason why the VH channel increases the number of measurement points when using the amplitude dispersion (D_A) as selection criterion. Results obtained over three geographical locations show that the VH channel helps in two ways. In the first place, the mean amplitude is increased for targets which have higher amplitude in VH channel, usually associated with rotated elements in the scene. In second place, and more importantly, the amplitude dispersion is decreased over many areas for which the VV channel exhibits fluctuations and peaks. Thanks to the insensitivity of the VH channel to these scene changes, it provides additional measurement points which are reliable despite their low amplitude. The increment of measurement points not only extends the spatial density and enables the detection of active deformation areas not found in the VV results but also provides more accurate results than only using the VV channel, thanks to the increased density of points, which helps the deformation estimation.**

***Index Terms*—Deformation, persistent scatterer interferometry (PSI), polarimetry, sentinel-1.**

I. Introduction

PERSISTENT scatterer interferometry (PSI) is established as a family of powerful techniques for remotely monitoring displacements of the Earth surface [1], [2], [3], [4]. It is based on the exploitation of interferogram stacks formed with time series of synthetic aperture radar (SAR) images acquired by satellites. In this context, the consistent and reliable acquisition scheme provided by Sentinel-1 (S1), also characterized by a short revisit time, has served to expand the use of this technique and to implement operational services and tools based on its data, e.g., EGMS [5], [6]. S1 is a constellation of two C-band SAR satellites, which belongs to the Copernicus Earth Observation Programme of the European Union.

Most of the examples of practical use of this technology employ images acquired at a single polarimetric channel (i.e., single-pol data), which is defined by setting the radar antenna for transmission and reception in the same polarization. However, since the launch of several satellites with extended polarimetric capabilities in the late 2000s, such as ALOS-PALSAR, Radarsat-2, COSMO-SKYMED, and TerraSAR-X, some efforts were conducted to study how the additional polarimetric channels measured by them could help improve the performance of PSI. For that purpose, Polarimetric PSI (PolPSI) approaches have been proposed and evaluated with dual-pol TerraSAR-X data [7], [8], [9], [10], [11], [12], [13], [14], dual-pol ALOS-PALSAR [14], quad-pol Radarsat-2 data [13], [15], [16], [17], [18], [19], and also recently with dual-pol S1 data [20], [21], [22].

All the proposed PolPSI algorithms aim at combining the data from the available polarimetric channels to improve the results provided by PSI. This combination is designed to optimize a cost function related to the pixel selection criteria (e.g., amplitude dispersion, average coherence) or to the phase quality of the selected pixels. In most cases, the improvement is demonstrated in terms of an increased spatial density of valid measurement points, i.e., the number of valid measurement points in the studied area is greater with PolPSI than in single-pol PSI.

In the particular case of S1, images are dual-pol, and the two polarimetric channels are VV and VH in the nominal acquisition mode over land. In one of the first works carried out on PolPSI with S1 data [21], the two channels were combined to optimize the amplitude dispersion index in urban areas and hence increase the number of PS candidates used as input to the Stanford Method for Persistent Scatterers (StaMPS) [23]. The resulting increase in pixel density over different urban units (i.e., commercial, industrial and residential) was analyzed.

Manuscript received 25 May 2022; revised 28 July 2022; accepted 9 September 2022. Date of publication 14 September 2022; date of current version 21 September 2022. This work was supported in part by the Spanish Ministry of Science and Innovation (State Agency of Research, AEI) in part by the European Funds for Regional Development under Projects PID2020-117303GB-C21 and PID2020-117303GB-C22, and in part by the framework of the ESA-MOST China DRAGON-5 project with ref. 59339.

Jiayin Luo and Juan M. Lopez-Sanchez are with the Institute for Computer Research, University of Alicante, E-03080 Alicante, Spain (e-mail: luo.jiayin@ua.es; juanma-lopez@ieee.org).

Francesco De Zan is with the Remote Sensing Technology Institute, German Aerospace Center, 82234 Wessling, Germany (e-mail: francesco.dezan@dlr.de).

Jordi J. Mallorqui is with the CommSensLab, Universitat Politecnica de Catalunya, 08034 Barcelona, Spain (e-mail: jordi.joan.mallorqui@upc.edu).

Roberto Tomás is with the Department of Civil Engineering, University of Alicante, E-03080 Alicante, Spain (e-mail: roberto.tomas@ua.es).

Digital Object Identifier 10.1109/JSTARS.2022.3206550

Another work based on S1 data [20] was aimed at optimizing the temporal coherence by properly combining the two channels. In the end, an increase of pixel density was found, together with an overall temporal coherence better than the one provided by the VV channel alone. More recently, the PolPSI optimizations of amplitude dispersion, average coherence, and a spatially adaptive method, were evaluated with S1 data in three different sites of China [22]. An improved performance was obtained in terms of pixel density and less noisy interferometric phase, which led to more detailed and reliable deformation maps. The main conclusion of that study was that it is worth processing the two channels of S1 data by applying PolPSI techniques, despite the added computational burden with respect to using only the VV channel.

Despite these apparent advantages, to date all institutions working on official motion surveys and companies providing deformation monitoring products directly discard the VH channel. This study advocates for the adoption of PolPSI also with S1 data and, hence, to keep and exploit the VH channel. For this purpose, we first revisit the roots of the contribution of the VH data and try to answer the following questions.

1) How does the VH channel in S1 data help increase the PS density? In other words, is it just because there are oriented features in the scene which return more power in this channel than in VV?
2) Are the PolPSI results with S1 data really better than single-pol PSI results? To what extent is there an improvement?
3) Is the contribution general for different scenarios or just particular of some cases?

In order to answer these questions, we focus this study on the physical interpretation of the optimization process carried out with the amplitude dispersion criterion. The amplitude dispersion index (D_A) is defined as the ratio of the standard deviation of the amplitude time series over the mean amplitude. Therefore, it can be improved in two ways: 1) increasing the mean amplitude or/and 2) decreasing the variance of the amplitude. We can anticipate that the VH channel, and the polarimetric optimization, may have significant influence on these two aspects depending on the scene properties.

The study is carried out over three test sites in Spain (Barcelona, Murcia, and Alcoy) characterized by very different urban features and deformation issues.

II. Formulation

The S1 data of each date comprises two images which correspond to the VV and VH channels. The set of S1 data acquired over the same geographical location during the observation interval was preprocessed using ESA SNAP[1] software with the following steps: 1) application of orbit files, 2) TOPSAR-Split, 3) radiometric calibration, 4) coregistration (with enhanced spectral diversity), 5) deburst, 6) subset, and 7) stack generation. All the dual-pol images forming the stack were coregistered with respect to a primary image.

[1][Online]. Available: https://step.esa.int/main/toolboxes/snap/

A. Polarimetric SAR Interferometry

For each pixel in a S1 image, a vector $\boldsymbol{k}$ is defined as

$$\boldsymbol{k} = \left[\ S^{VV}, S^{VH}\ \right]^T \tag{1}$$

where S^{VV} stands for the vertical copolar channel, S^{VH} is the crosspolar channel, and T is the transpose operator. With the help of a complex column vector $\boldsymbol{\omega}$, PSI methods can project each vector $\boldsymbol{k}$ into a new scalar μ [24]. As a result, the two polarimetric channels are combined as a new channel which is expressed as

$$\mu = \boldsymbol{\omega}^{*T}\boldsymbol{k} \tag{2}$$

where $*$ represents the conjugate operator.

To avoid introducing a variable phase term, $\boldsymbol{\omega}$ is forced to be identical for all images in one dataset. This constraint is usually named as equal scattering mechanism (ESM) [25].

The projection vector $\boldsymbol{\omega}$ can be expressed in many forms. The first version was introduced in [24], which has been used in most PolPSI studies [7], [8], [22]

$$\boldsymbol{\omega}^{*T} = \left[\ \cos(\alpha),\ \sin(\alpha)e^{j\theta_1}\ \right], \quad \begin{cases} \alpha \in [0, \pi/2] \\ \theta_1 \in [-\pi, +\pi). \end{cases} \tag{3}$$

In addition to expressing $\boldsymbol{\omega}$ by two angles, α and θ_1, we can also define it by using one angle θ_1 and one real number x_1

$$\boldsymbol{\omega}^{*T} = \left[\ 1 - x_1,\ x_1 e^{j\theta_1}\ \right], \quad \begin{cases} x_1 \in [0, 1] \\ \theta_1 \in [-\pi, +\pi). \end{cases} \tag{4}$$

Finally, as it was proposed in [18], we could use the following expression of $\boldsymbol{\omega}_{\text{initial}}$:

$$\boldsymbol{\omega}_{\text{initial}}{}^{*T} = \left[\ 1,\ x_1 e^{j\theta_1}\ \right], \quad \begin{cases} x_1 \in [0, \infty) \\ \theta_1 \in [-\pi, +\pi) \end{cases} \tag{5}$$

in which the real number x_1 ranges from 0 to ∞. In this last case, the normalization to make it unitary provides the following expression:

$$\boldsymbol{\omega}^{*T} = \frac{1}{\sqrt{1 + {x_1}^2}}\boldsymbol{\omega}_{\text{initial}}{}^{*T} = \frac{1}{\sqrt{1 + {x_1}^2}}\left[\ 1, x_1 e^{j\theta_1}\ \right]. \tag{6}$$

After defining the projection vector $\boldsymbol{\omega}$, we search for the optimum parameters in $\boldsymbol{\omega}$ to minimize the selection criterion D_A, which is calculated for the whole stack of single look images. We choose D_A because, compared with multilook data, single-look data are more sensitive to geometrical features that affect the polarimetric response. D_A is defined as [7]

$$D_A = \frac{\sigma_a}{\bar{a}} = \frac{1}{\overline{|\boldsymbol{\omega}^{*T}\boldsymbol{k}|}\sqrt{N-1}}\sqrt{\sum_{i=1}^{N}(|\boldsymbol{\omega}^{*T}\boldsymbol{k}_i| - \overline{|\boldsymbol{\omega}^{*T}\boldsymbol{k}|})^2} \tag{7}$$

where σ_A and $\bar{a}$ are the standard deviation and the mean value of image amplitude, respectively. N is the number of images in the time series, and the overline indicates the empirical mean value. Points with D_A lower than an established threshold will be selected as persistent scatterer candidates (PSC).

B. Optimization Method Based on SNR

A search method based on SNR optimization was first proposed in [18], but only applied with average coherence criteria. The core of the SNR-based method is that, in the vast majority of cases, the higher the SNR, the lower the D_A, or the higher average coherence, for deterministic scatterers. For dual-pol data, the values measured at the two channels in one acquisition can be expressed as

$$S^{VV} = S^{VV}_{\text{signal}} + S^{VV}_{\text{noise}} = y_0 e^{j\alpha_0} + n_0 \tag{8}$$

$$S^{VH} = S^{VH}_{\text{signal}} + S^{VH}_{\text{noise}} = y_1 e^{j\alpha_1} + n_1 \tag{9}$$

where S^{VV}_{signal} and S^{VV}_{noise} are the signal part and noise part of the VV channel, respectively, and equivalently for the VH channel in (9). With (8) and (9), we can rewrite vector $\boldsymbol{k}$ as the addition of two parts

$$\boldsymbol{k}_{\text{signal}} = \left[\ y_0 e^{j\alpha_0}, y_1 e^{j\alpha_1}\ \right]^T \tag{10}$$

$$\boldsymbol{k}_{\text{noise}} = \left[\ n_0, n_1\ \right]^T. \tag{11}$$

It should be noted that α_0 and α_1 are not related to α in (3). They are used for consistency with the original reference.

In the SNR-based method, $\boldsymbol{\omega}$ was defined by (6). But in this section, for the convenience of introducing the algorithm, we use $\boldsymbol{\omega}_{\text{initial}}$ instead of $\boldsymbol{\omega}$. However, the normalization is still necessary during the computation of the interferograms.

Then, according to (2) and (5), we have

$$\begin{aligned}\mu_{\text{signal}} &= y_0 e^{j\alpha_0} + x_1 y_1 e^{j(\alpha_1+\theta_1)} \\ &= A e^{j\beta}\end{aligned} \tag{12}$$

$$\mu_{\text{noise}} = n_0 + x_1 n_1 e^{j\theta_1} \tag{13}$$

where A is the amplitude of μ_{signal} and β is the phase. The power of μ_{signal} results in $\mu_{\text{signal}(p)} = A^2$. Under the assumption that the noise is independent of the signal, and $n_0, n_1 \sim N(0, \sigma^2)$, the power of noise can be obtained as $\mu_{\text{noise}(p)} = (1 + x_1^2)\sigma^2$.

From the definition of SNR, we can obtain the following expression:

$$\text{SNR} = \frac{\mu_{\text{signal}(p)}}{\mu_{\text{noise}(p)}} = \frac{A^2}{(1 + x_1^2)\sigma^2} \tag{14}$$

in which, if we fix the value of x_1, $\mu_{\text{noise}(p)}$ will be independent of θ_1. From (12) and (14), SNR reaches its maximum value when $\alpha_0 = \alpha_1 + \theta_1$, hence the optimum θ is defined as

$$\theta_{1\,(\text{opt})} = \alpha_0 - \alpha_1. \tag{15}$$

As a result, the strategy of finding the optimum $\boldsymbol{\omega}$ consists in first setting an initial value of x_1 and then optimizing θ_1. Secondly, using the obtained $\theta_{1\,(\text{opt})}$, the value of x_1 is optimized within the search space. More details are introduced in [18].

Once the optimum projection vector $\boldsymbol{\omega}$ is found, we form a series of new single look complex (SLC) images which contains the information of all available polarimetric channels.

Compared with the typical numerical algorithms employed for optimization, like the exhaustive search polarimetric optimization (ESPO), the SNR optimization is much more efficient from the computational point of view, although the advantage is much more evident for quad-pol data than for dual-pol data. In addition, the SNR-based method is helpful to understand the optimization process from the perspective of the scene properties.

One may suggest a simpler alternative procedure consisting of merging the PS candidates from both VV and VH channels after being processed independently. That merging method without a polarimetric optimization is not discussed in this work because it was already studied in the original works on polarimetric PSI [15], [17], [26], and it yields a number of PSs much smaller than when the optimization is applied.

C. Ground Deformation Estimation

After the polarimetric optimization, any interferogram resulting from a combination of two of the available new SLC images can be obtained through

$$I = \mu_1 \mu_2^*. \tag{16}$$

In this study, the employed PSI processing method is known as coherent pixels technique (CPT) [27], [28], which is based on the use of a set of interferograms characterized by low temporal or geometrical decorrelation. The interferograms to be computed are selected by defining two sets of thresholds for spatial and temporal baselines. The first set includes interferograms with a short temporal baseline (less than 40 days) and long perpendicular baseline (up to 400 m). The second set includes interferograms with a long temporal baseline (up to 365 days) and short perpendicular baseline (less than 50 m). This selection criterion ensures diversity of baselines and avoids interferograms with extreme decorrelation. Once the interferograms are selected and computed, the PSI processing can be carried out using the same algorithms as for the single-pol case.

All those pixels exhibiting a $D_A < 0.25$ are selected as PSCs. Following the steps of CPT, the selected PSCs are linked by a Delaunay triangulation. The phase increment between two neighboring PSCs at the kth interferogram, $\Delta\phi^k_{dif}$, is expressed as a function of the increments of linear velocity Δv_{linear} and DEM error $\Delta\varepsilon$, which are constant for each link in all K differential interferograms. This phase model is used to retrieve Δv_{linear} and $\Delta\varepsilon$

$$\Delta\phi^k_{\text{model}} = \frac{4\pi B^k_\perp}{\lambda R \sin\alpha}\Delta\varepsilon + \frac{4\pi}{\lambda} T^k \Delta v_{\text{linear}} \tag{17}$$

in which, $B^k_\perp$ and T^k are the perpendicular and temporal baselines of interferogram k, R is the range distance to the target from the sensor, α is the local incidence angle, and λ is the central wavelength of the SAR pulses. The estimation of Δv_{linear} and $\Delta\varepsilon$ can be obtained through a maximization of the following cost function:

$$\Gamma = \frac{1}{K}\sum_k^K \left| e^{j(\Delta\phi^k_{\text{dif}} - \Delta\phi^k_{\text{model}})} \right|. \tag{18}$$

The maximization of Γ provides a pair of velocity and DEM error increments for each link between PSCs. To build the final PS set, links with Γ value below 0.5 are discarded, and isolated PSCs which are not connected to other PSCs are discarded as

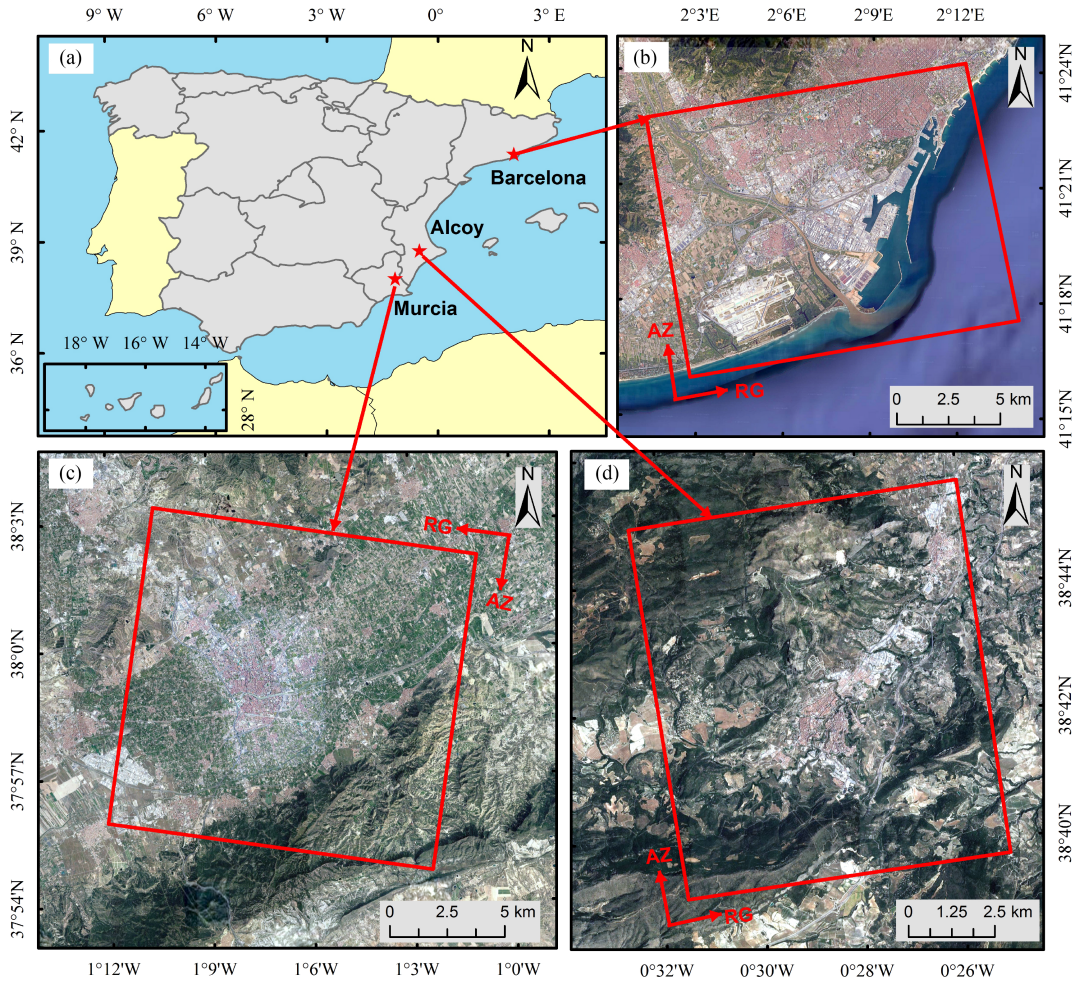

Fig. 1. Test sites. (a) Location of the three test sites in Spain, indicated by red stars. (b)–(d) Google Earth optical image over the Barcelona, Murcia, and Alcoy test sites, respectively. The red rectangle shows the frame of S1 subimage processed in this study.

TABLE I
MAIN CHARACTERISTICS OF THE S1 DATASETS

Test site	Barcelona	Alcoy	Murcia
Acquisition mode	Interferometric Wide-Swath		
Polarization	Dual-pol (VV,VH)		
Pixel dimensions	13.90 m × 2.33 m		
Orbit	Ascending	Ascending	Descending
Incidence angle	36.1°- 41.9°	41.5°- 46.0°	30.6°- 36.8°
Images	189	186	271
Time span (start)	12/2016	01/2017	01/2016
Time span (end)	01/2021	01/2021	01/2021
Intferograms	4200	4348	8037

well. As the number of PSC and PS affects the network formed and the deformation estimation, in Section IV-C we analyze the added value of the VH channel and the polarimetric optimization through the estimation of the Δv_{linear} and $\Delta\varepsilon$.

III. DATASET

Three dual-pol S1 datasets over different cities in Spain are exploited in this study. The location of the three study areas is shown in Fig. 1. The key parameters of the three datasets are listed in Table I.

The first dataset is formed by 189 images acquired from December 2016 to January 2021 over the urban area of Barcelona, NW, Spain. The processing has been applied over a section of the images with 4043×1089 pixels. A wide variety of scenarios are present in this region, i.e., airport, harbor, and urban areas which exhibit diverse orientations of streets and buildings with respect to the acquisition geometry. Ground deformation is expected over some areas due to settlement of recent constructions and in the harbor, as it has been reported in the past [17], [29].

The second area of interest corresponds to the town of Alcoy, in Alicante province (SE Spain). A set of 186 images of size 3182×674 pixels acquired from January 2017 to January 2021 is used for analysis. The area of Alcoy is characterized by the occurrence of frequent landslides caused by rainfall, anthropogenic activities, and earthquakes occurred in the past. The construction of recent buildings as well as the Alicante-Valencia A-7 highway has also lead to some settlements [30], [31], [32].

The last dataset consists of 271 images, acquired from January 2016 to January 2021, which cover the area of Murcia city (SE Spain). A section of image with 3339×988 pixels has been selected as a test area because it is known to be affected by land subsidence due to groundwater extraction [33], [34].

TABLE II
PERCENTAGE AND NUMBER OF SELECTED PSC AND PS FOR DIFFERENT CHANNELS: VV AND OPTIMUM (OPT)

	PSC	PS
Test site	Barcelona	
VV	1.29% / 56689	1.28% / 56395
OPT	2.99% / 131556 (+132%)	2.97% / 130712 (+132%)
Test site	Alcoy	
VV	0.36% / 7636	0.35% / 7473
OPT	0.84% / 18039 (+136%)	0.83% / 17764 (+138%)
Test site	Murcia	
VV	0.91% / 30457	0.91% / 30321
OPT	2.15% / 71109 (+133%)	2.14% / 70685 (+133%)

IV. RESULTS AND ANAYLSIS

A. Number of Pixels

In this first section, we compare the number of PSCs selected by the conventional VV channel and by the optimized channel (including the information of VV and VH) for the three test areas. As it was introduced in Section II-C, in all cases, a 0.25 D_A threshold has been used for selection of PSCs. Then, after removing links with $\Gamma < 0.5$, the final PSs with valid deformation measurements are obtained.

Table II shows the pixel density (percentage with respect to the total number of pixels) and pixel number before and after removing low phase quality PSCs. In all cases, with the polarimetric optimization the numbers of PSCs and final PSs are increased. The number of PSC points in the optimum channel has been increased by around 132, 136, and 133% compared with VV channel in Barcelona, Alcoy, and Murcia, respectively. Notably, the similar number of PSCs and PSs in all cases shows that most of PSCs survive as final PS points, which indicates that the interferometric phase quality of the optimized pixels, which were not selected in the VV channel, has been improved through the optimization process.

B. Associating the Increased PS Points With Physical Features

In order to understand how the VH channel in S1 data helps increase the PS density, we first analyze the difference of average amplitude in the VV, VH, and optimum (OPT) channels. The test area chosen for this initial analysis is Barcelona, a big city characterized by streets and buildings with diverse geometrical features and orientations.

The comparison of the mean amplitude of the PS points (all of them selected in the optimum case) is illustrated in Fig. 2. As expected, the image in Fig. 2(a) shows that the mean amplitude of the VV channel is higher than the VH channel in most areas. After the PolPSI processing, the mean amplitude in the optimum channel is increased significantly, so it is greater than the VV amplitude in many locations of the city. However, for more than half of the total selected pixels (57%, as shown in Table III) the mean amplitude provided by the VV channel is still higher than that of the optimum channel. In other words, the optimization is not always achieved by increasing the mean amplitude with respect to the VV channel. To prove that, the comparison maps of standard deviation are given in Fig. 2(b). The standard deviation of VV amplitude is greater than one of VH for most areas (around 97.6% shown in Table III). As a result, the optimization process not only works by searching for a higher final amplitude but also by favoring the stability of the amplitude, and this second feature is provided by the VH channel better than the VV channel.

TABLE III
PERCENTAGE AND NUMBER OF PS POINTS FOR MEAN AMPLITUDE AND STANDARD DEVIATION COMPARISON SHOWN IN FIG. 2

	Mean amplitude (Percentage/Number)	Standard deviation (Percentage/Number)
VV≤VH	15.3% / 20055	2.4% / 3119
VV>VH	87.7% / 110657	97.6% / 127593
VV≤OPT	42.2% / 55223	17.1% / 22366
VV>OPT	57.8% / 75489	82.9% / 108346

Note: That the increases of PSC and PS, expressed as percentages, are written into brackets.

TABLE IV
PS NUMBER FOR DIFFERENT CHANNELS OVER SIX SCENARIOS SHOWN IN FIG. 2 C

Area	A	B	C	D	E	F
VH	38	163	967	62	1511	517
VV	425	267	1308	73	1596	494
OPT	599	619	3273	154	4709	1156

To further explore the different optimization behaviors, we have marked six small areas in Fig. 2, which are labeled from A to F. In areas A to D there is a balance of pixels with higher amplitude in the VV or the optimum channels, whereas in areas E and F most of the pixels show a higher mean amplitude in the optimum channel than the VV one. The corresponding optical images are given in Fig. 2(c).

Regarding the first group of scene subsets, areas A and B are typical urban zones characterized by buildings with orientation parallel to the radar flight direction. Area C includes an industrial zone in which there is a chemical plant with cylindrical containers. Area D corresponds to two dikes of the harbor, formed by rocks. Generally, in these cases (A–D) the response of the VV channel is much higher than the VH channel, but the VH channel still contributes to increase the number of PS points, as it is demonstrated in Table IV. The second group is formed by areas E and F. In area E, part of the *Eixample* district in Barcelona, the orientation of the streets is not parallel to the radar flight direction, and the buildings are chamfered. Finally, area F corresponds to a portion of the access road to the airport. In areas E and F, the mean amplitude of the VH channel is even larger than that of the VV channel.

In order to explore the role of VH channel in the polarimetric optimization process, the histograms of the parameters x_1 and θ_1 that define the projection vector $\boldsymbol{\omega}$ are given in Fig. 3. Since the value of x_1 ranges from 0 to ∞, we have also shown the histogram of α, for which the relationship between x_1 and α according to (3) and (6) is given by the following expressions:

$$\cos(\alpha) = \frac{1}{\sqrt{1+{x_1}^2}} \tag{19}$$

$$\sin(\alpha) = \frac{x_1}{\sqrt{1+{x_1}^2}} \tag{20}$$

$$\alpha = \arccos\left(\frac{1}{\sqrt{1+{x_1}^2}}\right) = \arcsin\left(\frac{x_1}{\sqrt{1+{x_1}^2}}\right). \tag{21}$$

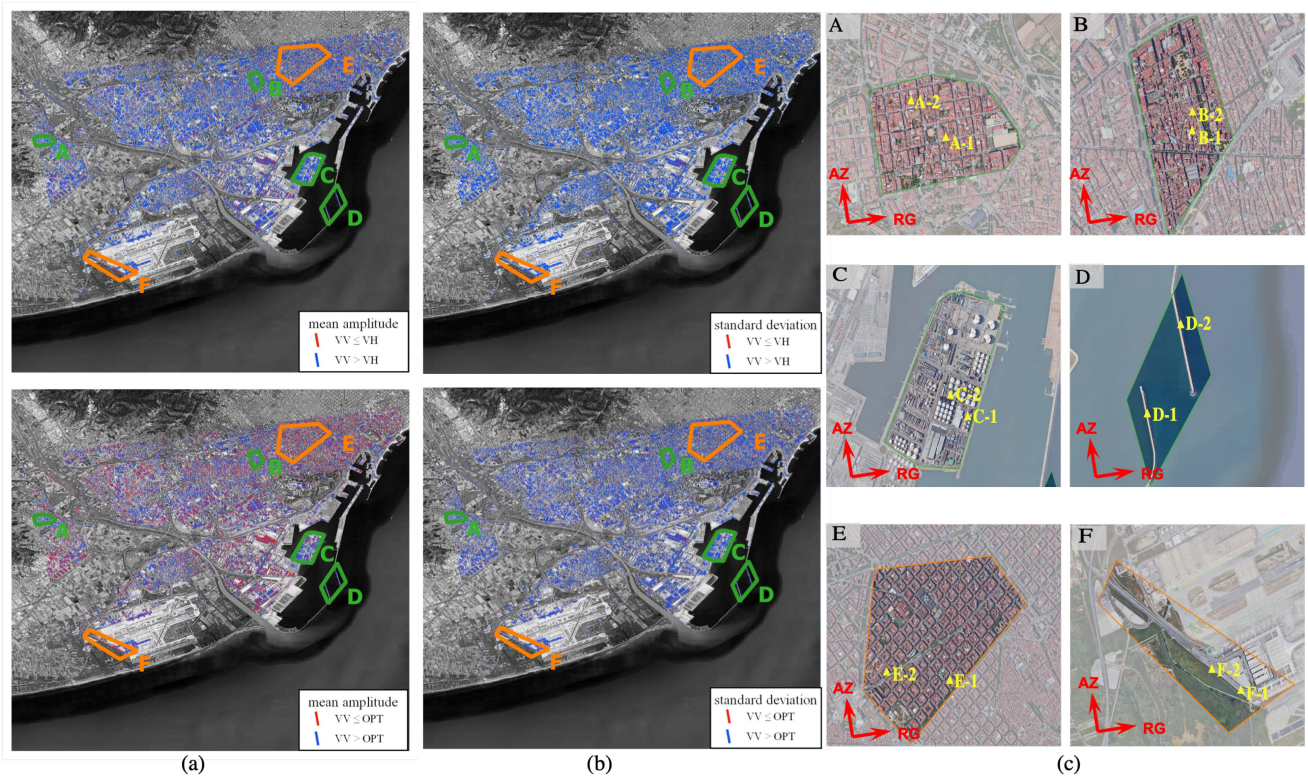

Fig. 2. Difference of (a) mean amplitude and (b) standard deviation map in Barcelona for VV and VH channel, VV and optimum channel, for all the PS points selected after the optimization. Some areas with high mean amplitude value in the VV channel are highlighted by green polygons, whereas orange polygons indicate areas where amplitude in VV channel is lower than the optimum channel. (c) Optical image inside these polygons.

TABLE V
STATISTICS OF THE SELECTED PS POINTS SHOWN IN FIG. 4 AND FIG. 5

Pixel		A-1	A-2	B-1	B-2	C-1	C-2	D-1	D-2	E-1	E-2	F-1	F-2
	VH	0.35	0.36	0.54	0.24	0.19	0.21	0.22	0.21	0.23	0.48	0.19	0.13
D_A	VV	0.27	0.26	0.28	0.26	0.50	0.65	0.28	0.32	0.45	0.26	0.54	0.48
	OPT	0.23	0.20	0.21	0.21	0.18	0.20	0.20	0.21	0.24	0.25	0.18	0.12
	VH	0.17	0.22	0.26	0.50	0.96	0.56	0.18	0.28	0.52	0.27	0.37	0.68
Mean amplitude	VV	1.17	2.33	1.08	1.68	1.20	5.71	0.49	0.61	0.48	1.15	0.15	0.25
	OPT	0.46	0.64	0.66	0.73	0.96	0.56	0.23	0.29	0.52	0.98	0.35	0.69
	VH	0.06	0.08	0.14	0.12	0.18	0.12	0.04	0.06	0.12	0.13	0.07	0.09
Standard deviation	VV	0.32	0.58	0.30	0.43	0.60	3.70	0.14	0.19	0.22	0.30	0.08	0.12
	OPT	0.10	0.13	0.14	0.17	0.20	0.12	0.05	0.06	0.12	0.24	0.07	0.09
x_1	OPT	3.75	4.60	2.01	4.85	14.44	83.13	5.59	54.04	19.37	0.67	3.67	7.95
$\alpha(^\circ)$	OPT	75	78	64	79	86	89	80	89	87	34	75	83
$\theta(^\circ)$	OPT	-19	2	-183	-38	66	-123	-32	2	-155	-7	-57	132

It is clear that α is greater than 45° in the majority of pixels included in these polygons, which means that VH has greater weight than VV when constructing the optimum channel. Instead, θ_1 does not present any trend or dominant value here. This angle is a phase difference between the two weights applied to the two components of the received wave [35].

The behavior of the polarimetric optimization can be better interpreted by analyzing the amplitude time series of typical pixels in the different selected areas. Therefore, in each area, according to the amplitude level we have selected two pixels for analysis. The histogram and time series of the amplitude at the three channels (VV, VH, and optimum) are shown in Figs. 4 and 5.

For the pixels included in areas A to D (Fig. 4), there are two general differences in the amplitude distribution when comparing the VV and the optimum channel. First, the width of the distribution is decreased by the optimization, which means the dispersion is decreased. Second, the optimum distribution of amplitudes is shifted to lower values, which indicates a decrease in the average amplitude. Therefore, in these pixels, the optimization entails a decrease of both numerator and denominator of the amplitude dispersion index. But, since the final index is smaller than the original one (because it has been optimized), the decrease in dispersion is more relevant than that of the mean amplitude. For a more comprehensive analysis, we list the key values of these points in Table V. The α value at points C-1

Fig. 3. Histograms of (a) x_1, (b) α, and (c) θ_1 for all the PS points selected after the optimization in the six scenarios defined in Fig. 2(c).

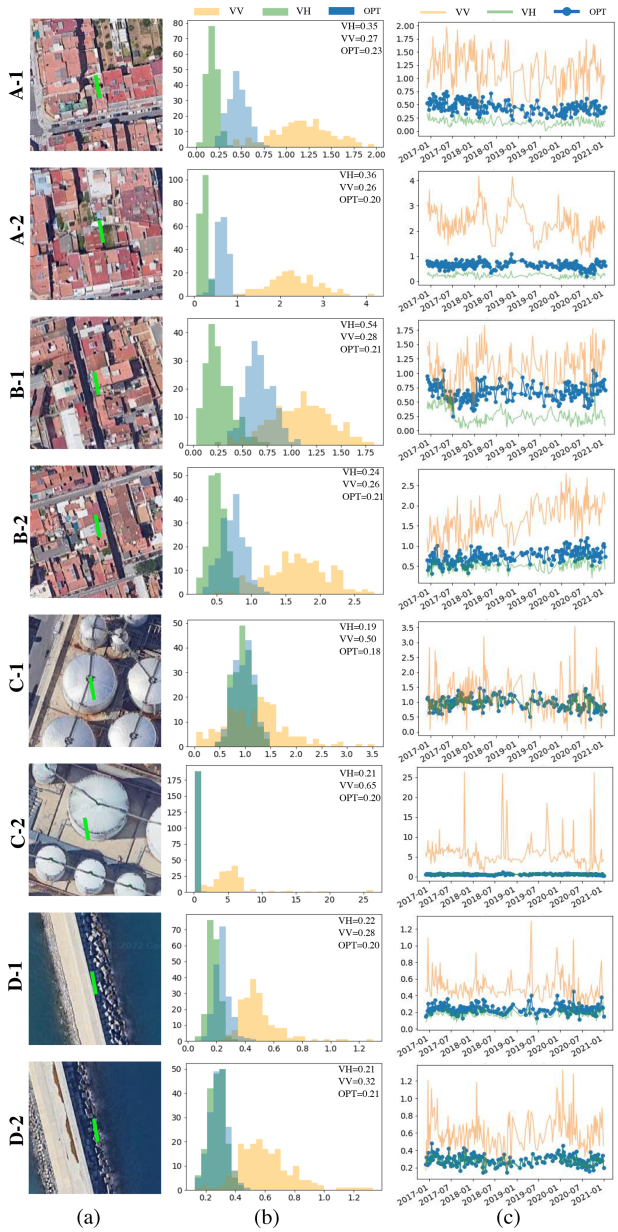

Fig. 4. Selected pixels in areas A-D. (a) Corresponding ground target on optical image. (b) Histogram of amplitude and D_A value for each channel. (c) Time series of amplitude. Color code: optimum (blue), VV (yellow), and VH (green).

and C-2 is almost 90° because the optimum channel is virtually equal to VH channel. It is also clear that the improvement of D_A comes from the decrease of dispersion.

From the amplitude time series in Fig. 4 and values in Table V, it can be concluded that the VV channel is prone to exhibit strong fluctuations in its amplitude, which in some cases seem seasonal (e.g., for pixel A-2) and in other cases are affected by isolated peaks (e.g., in pixels C-1, C-2, and D-1). These peaks may come from changing elements in the scene, like cars, which are present in roads and streets in some images, or windows in buildings, which can be open or closed, hence varying clearly their response [36]. It is worth to note that, since the dates with peaks change from pixel to pixel, discarding the acquisitions with peaks would not be a good solution for reducing the fluctuations, since it would entail a complex processing in later steps. In addition, even if we remove the acquisitions with peaks, for pixels with similar mean amplitude in VH and VV channels, like C-1, the standard deviation of the remaining values in the VV channel is likely to be higher than at the VH channel. Thus, the improvement for D_A is not obvious and one cannot guarantee C-1 would be a PS. Contrarily, the amplitude of the VH channel is by far more stable in all cases. Therefore, the VH channel offers an enhanced stability in the pixel reflectivity which can be exploited by PolPSI to provide an effective deformation measurement in locations which otherwise (i.e., using only the VV channel) would be ignored due to their obvious fluctuating radar response.

The amplitude distribution and time series of the pixels chosen in areas E and F are shown in Fig. 5. Pixel E-1 is characterized by a similar mean amplitude in both VV and VH channels, but the dispersion of the VH channel is much smaller than that of VV. As a result, the optimized channel resembles VH and provides a much lower dispersion index than the VV channel (0.24 instead of 0.45) which falls below the selection threshold (see Table V). Regarding pixel E-2, the α value is less than 45 degrees and the optimum channel is very similar to VV because the VH channel amplitude fluctuates and does not improve the performance of the VV channel. In this case, the optimization is able to reduce

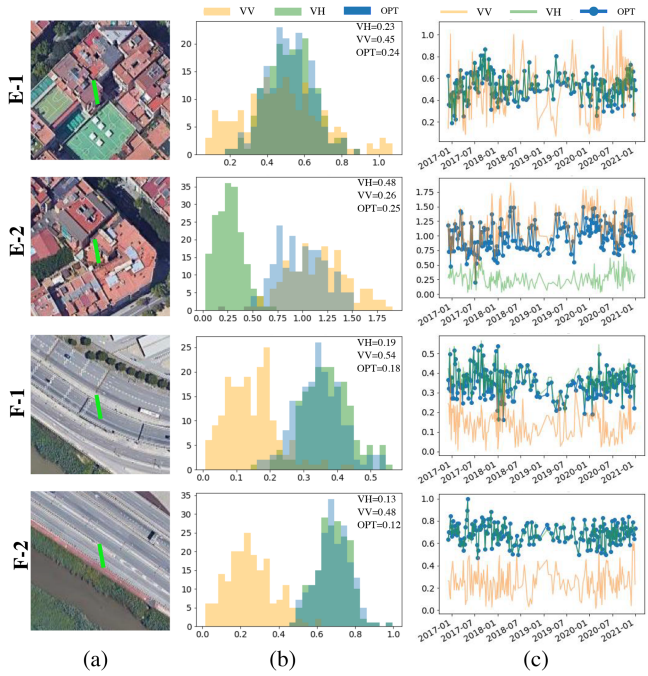

Fig. 5. Selected pixels in areas E and F. (a) Corresponding ground target on optical image. (b) Histogram of amplitude and D_A value for each channel. (c) Time series of amplitude. Color code: optimum (blue), VV (yellow), and VH (green).

only marginally the dispersion index (from 0.26 to 0.25), hence not providing a significant improvement. The situation is quite different in pixels F-1 and F-2. In this case, the dispersion of the VV and VH amplitudes are similar, but the mean amplitude of the VH channel is much larger than the VV channel due to the orientation of the scattering elements in the scene (barriers along the airport access road). Therefore, only in this last case the optimization is due to an increased mean amplitude. Therefore, it can be concluded that the working principle of PolPSI depends on the power of the VH channel, which is a function of the imaged objects. When the mean amplitude of VH is higher than VV, the polarimetric optimization improves D_A by increasing the mean amplitude value. This is the case of roads and buildings which are not parallel to the flight direction. When the mean amplitude of VH is lower than VV, VH channel can also importantly contribute to the optimization process by exploiting its lower sensitivity to response changes from some targets (like rocks, cylindrical containers, and buildings with orientation similar to the radar flight direction) whose reflected signal notoriously fluctuates at the VV channel. Despite the low mean amplitude for the optimized pixels, PSCs obtained by this optimization are rarely discarded after the phase analysis in CPT, so they are actually persistent scatterers contributing effectively to enhance the deformation estimation.

C. Deformation Results

Deformation results have been generated over the three test sites by means of the CPT procedure (Section II-C) using separately the VV and the optimum channel for comparison purposes. Fig. 6 shows the histograms of the estimated DEM error and linear velocity in different selected PS groups. For Murcia and Barcelona, both VV and optimum channel provide the same patterns, which correspond to zero-mean Gaussian distributions, as expected in areas which are mostly stable (without deformation). However, in the relatively small town of Alcoy, the histograms of both DEM error and velocity in VV channel do not follow a Gaussian distribution with zero-mean. In this site, the optimum channel provides distributions for both variables whose average is closer to zero than with the VV channel. This is a direct consequence of the sparsity of the network built by linking all selected pixels. The lower density of pixels of the VV channel entails less reliable estimates than for the optimum channel.

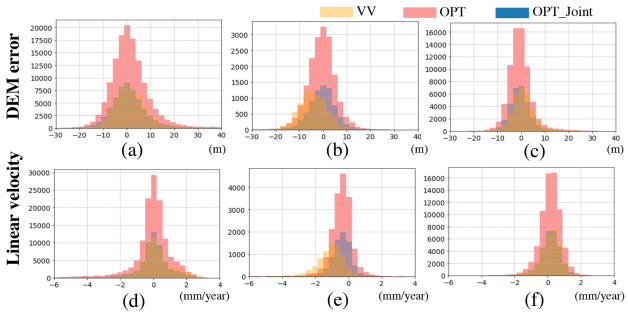

Fig. 6. Histograms of estimated linear velocity and DEM error for PS points selected in VV or OPT channel. Joint means PS points selected both in VV and OPT channel. (a) and (d) for Barcelona, (b) and (e) for Alcoy, (c) and (f) for Murcia.

Figs. 7, 8, and 10 show the deformation velocity maps obtained for the three test sites by using both the VV channel and the optimum one. The increased PS density provided by PolPSI helps adding new measurement points to existing deformation areas and/or revealing new deformation areas which are not present in VV channel results. This is analyzed further separately for each site.

1) Results in Barcelona: The main deformation areas of Barcelona are located in the harbor and the airport, which are also near the coast (see yellow rectangles in Fig. 7), whereas the city centre is stable. This result is in accordance with previous studies [13], [15], [16], [17], [29].

In the central column of Fig. 7, we show the distribution of PS points for four marked regions. B1 and B2 represent areas in which the amplitude of the VV channel is much higher than that of VH channel, while B3 and B4 are areas which have higher amplitude in the VH channel. It is clear to see that PolPSI can effectively improve the density of points, independently of the different optimization reasons found in B1–B2 and B3–B4. In B1, B2, and B3, the deformation rate values in the added PS points are consistent with the values shown in the VV channel, so they contribute only by extending the measurement coverage. In the case of B4, however, a new deformation area can be detected by adding the information of the VH channel, which was not detected in the deformation map derived from VV data.

2) Results in Alcoy: In Alcoy, all deformation areas are quite isolated and correspond to landslides and consolidation settlements over small clusters (see Fig. 8). As we commented

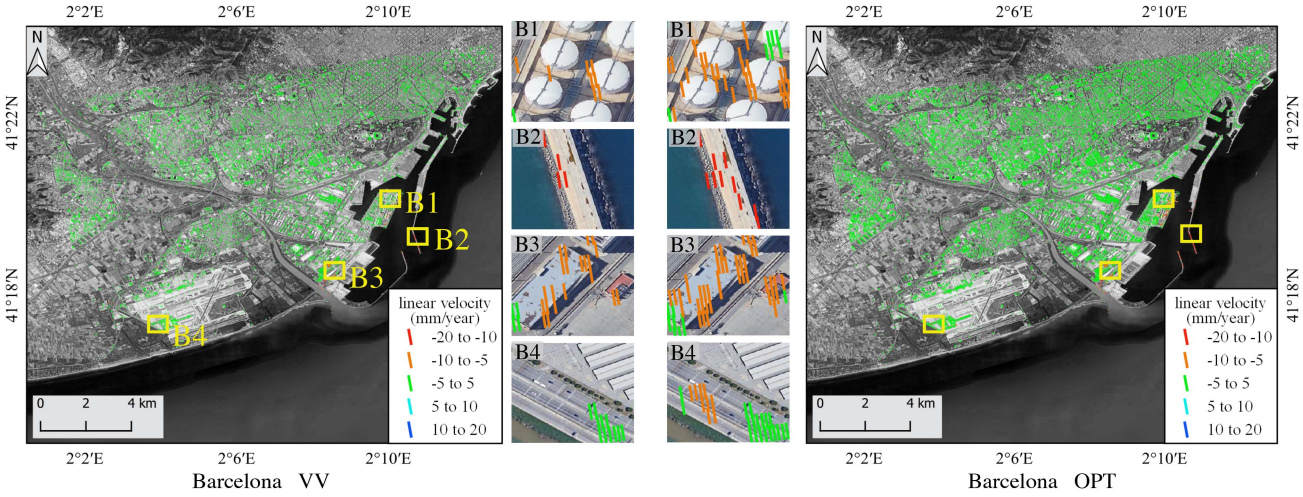

Fig. 7. Linear velocity maps for VV and OPT channels over Barcelona.

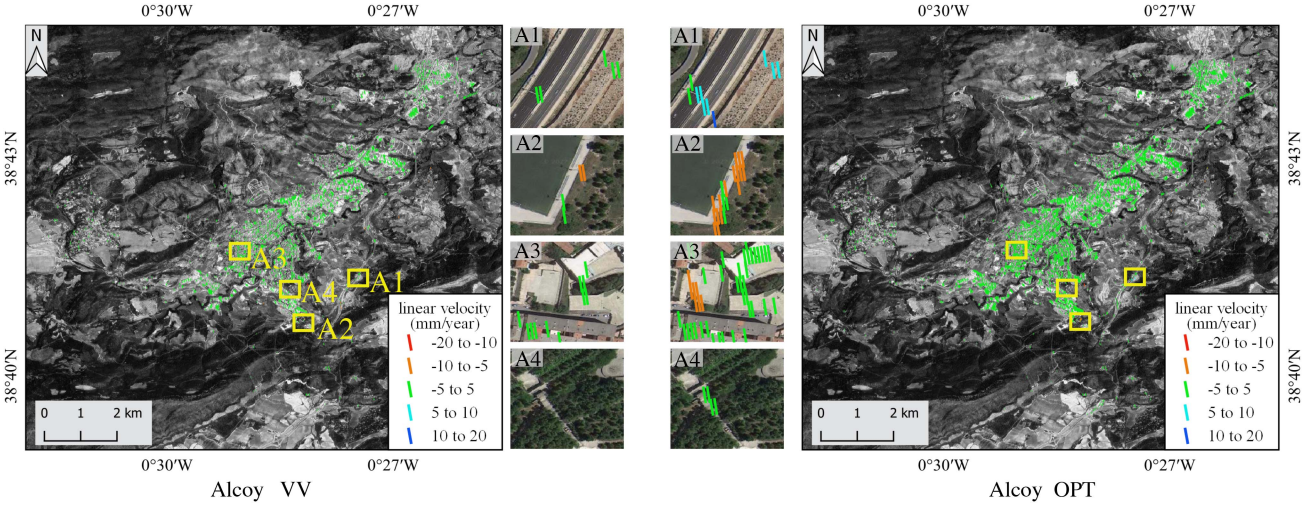

Fig. 8. Linear velocity maps for VV and OPT channels over Alcoy.

previously, due to the increased density of pixels when using the optimum channel, the deformation estimates are more reliable than with the VV channel alone. An example of this behavior is shown in area A1, which corresponds to a known landslide affecting a recently built highway. In the optimum channel, PS points exhibit positive deformation rates from 5 to 20 mm/year, whereas in the VV channel the results do not exceed 5 mm/year. Deformation is measured along the line of sight (LOS), and positive values mean movements toward the satellite, whereas negatives values correspond to movements away from the sensor.

This landslide is known by the authorities and is being monitored. Control points were placed on the wall, at different horizontal positions and also at different heights for the same horizontal position. Absolute displacements along the three Cartesian axes are being measured at each control point since April 2017. The four control points (vertically arranged over the same position in the wall) which are closest to the PS points in area A1 are shown in Fig. 9. For comparison purposes, the displacement rate measured in situ from April 2017 to April 2021

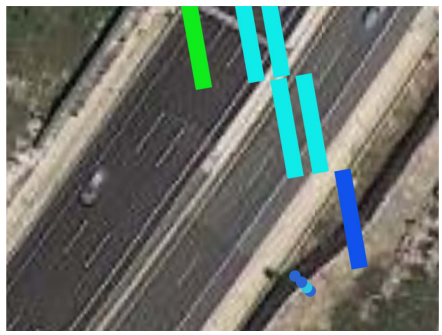

Fig. 9. Location of control points in Alcoy. The four control points closest to area A1 are marked by circles. The color represents the same linear velocity intervals used in Fig. 8.

was obtained at the four points and averaged. The resulting 3-D displacement rate was then projected along the LOS direction according to the transformation employed in [37]. The resulting average deformation rate was 10.04 mm/year, which is very

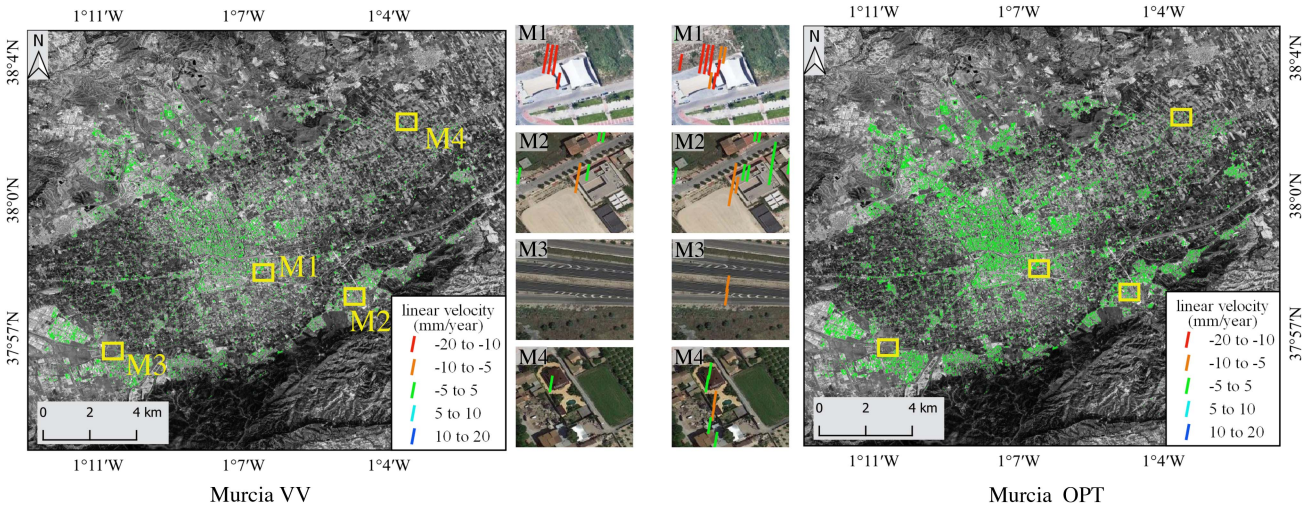

Fig. 10. Linear velocity maps for VV and OPT channels over Murcia.

similar to the value obtained at the dark blue PS point in Fig. 9 (measured at the optimum channel) which is 11.69 mm/year.

In area A2, the optimum channel is able to provide additional measurement points over the deformation area of the crown of a landslide already detected in the VV channel. Contrarily, results from the optimum channel in area A3, affected by constructive settlements, provide the detection of an active deformation area which was missing in the VV channel. Finally, in area A4 we find some stable pixels over a site in which the VV channel did not provide any measurement point.

3) Results in Murcia: The improvement provided by the combination of the two channels can be observed also in Murcia (Fig. 10). The added measurement points in areas M1 and M2 behave as the ones obtained by the VV channel alone, so in these active zones (-10 to -5 mm/year) there is an increased spatial coverage. In addition, the optimum channel also can find some new active deformation areas, not retrieved by the VV channel, as the ones shown in locations M3 and M4.

V. Discussion

We first review in this section the contribution of this work with respect to previous PolPSI studies with S1 data [20], [21], [22]. The general findings about the increase in pixel density, and hence spatial coverage of the deformation results, are in agreement with the results already published. The number of pixels in the optimum case is around 130% above the amount obtained by using VV alone, provided by that the amplitude dispersion index is used as selection criterion, whereas an increase between 80% and 170% was found in previous studies, depending on the test site.

Regarding the deformation results provided by the optimized polarimetric channel, we have found that the increased number of pixels helps find new active deformation areas which are missed by the VV data. In addition, as it was also shown in [22], the deformation rate can be estimated more accurately thanks to the increased pixel density. In our tests, this was especially helpful in the case of Alcoy, since this area exhibited the lowest density of PS among all test sites.

Apart from the extended assessment from the point of view of the improved final results, the main novelty of this work consists in the illustration and physical interpretation of the behavior of the scene response that contributes to the selection of additional pixels when the VH channel is included and when the polarimetric optimization is adopted. We have found that there are basically two cases in which PolPSI enhances the pixel selection stage. The first and most expected case corresponds to pixels in which there are scattering elements (buildings and infrastructures) rotated with respect to the incidence direction. This arrangement in the scatterers induces a high level in the cross-polar signal, as it is well known in the polarimetric community [38], [39]. As a result, if the VH amplitude is high and stable and the VV is not, this type of pixels is selected. The second case of enhanced selection is perhaps more surprising than the first one and has been analyzed in more depth. We have found many pixels in which the amplitude of the VV channel is high but unstable, showing fluctuations and peaks as a consequence of the presence of changing elements in the scene. Contrarily, the VH channel exhibits a much lower amplitude and it is not subject to such fluctuations. Therefore, the much lower dispersion of this channel helps the optimization find a signal with good properties (i.e., phase stability) for the PSI processing. We have found many examples in which the optimization chooses a combination of VV and VH signals with low and stable amplitude. It is worth to note that the subsequent PSI processing carried out over these pixels has demonstrated that they show phase quality as the rest of pixels of other types.

Finally, in this work we have also applied for the first time the SNR-based optimization [18], [19] to minimize the amplitude dispersion, instead of optimizing the average coherence. This method shows a reduced computational burden with respect to the conventional ESPO method [15] because the 2-D search for optimum coefficients is transformed into two sequential 1-D searches. Comparative results are given in [18].

This work has been focused on PolPSI applied to urban areas, in which amplitude dispersion is the common selection criterion to identify PS. The extension to nonurban areas entails the joint use of PS and DS (distributed scatterers) because PS

are mainly located in urban areas. The first consequence of adding DS is that instead of using the amplitude dispersion as selection criterion another criterion is needed. In that context, the average coherence is usually the first choice. The performance of PolPSI based on coherence optimization has been already studied [15], [17]. In a recent study [22], three experiments were conducted over urban and nonurban areas to prove the effectiveness of PolPSI with amplitude dispersion, with average coherence, and with the combination of both. The density of final deformation monitoring pixels was improved compared to (single-pol) conventional PSI techniques in all three test sites. A possible analysis to be carried out is the physical interpretation of the optimization, which is, by definition, entirely different to the amplitude dispersion optimization. A second aspect to be analyzed is the selection of homogeneous pixels for adaptively defining the DS. The contribution of dual-pol S1 data in this context, and the physical interpretation of the performance achieved constitute subjects of future research in this topic.

VI. Conclusion

The contribution of PolPSI on S1 data by using the amplitude dispersion as PS selection criterion has been investigated in this work. The tests carried out have allowed us to answer the questions stated in the Introduction as follows.

1) *How does the VH channel in S1 data help increase the PS density? In other words, is it just because there are oriented features in the scene which return more power in this channel than in VV?* We have seen that there are two cases in which the VH data contribute to improve the PS density. The first correspond to scatterers rotated with respect to the incidence plane, for which the VH response is high. The second case, which is more frequent, corresponds to pixels in which the VH amplitude is low but stable. With the help of PolPSI, the VH channel in the second case can contribute by avoiding peaks and fluctuations present in the VV channel, thus enabling the selection of pixels with good quality which would not have been identified if only VV data were processed.
2) *Are the PolPSI results with S1 data really better than single-pol PSI results? To what extent is there an improvement?* The improvement with respect to the single-pol case is multifold: a) pixel density, and hence measurement coverage, is increased by about 130%, b) new active deformation areas can be found in locations in which the VV channel did not provide measurements, and c) more reliable estimates are found with algorithms like CPT for which the density of the pixel linking network has a strong impact in the estimation of the displacements.
3) *Is the contribution general for different scenarios or just particular of some cases?* The improvement has been found in three urban areas in different geographical locations and characterized by different physical properties and deformation phenomena. Therefore, the contribution is always clear, although the improvement magnitude depends on the scenario.

In summary, on the basis of the analysis carried out, it is worth keeping the data of the VH channel and using PolPSI for a better displacement measurement.

Acknowledgment

The authors would like to thank Mr. Juan Jiménez, engineer of the Ministry of Transport, Mobility and Urban Agenda, for providing the monitoring data over Alcoy used in this work.

References

[1] A. Ferretti, C. Prati, and F. Rocca, "Permanent scatterers in SAR interferometry," *IEEE Trans. Geosci. Remote Sens.*, vol. 39, no. 1, pp. 8–20, Jan. 2001.
[2] A. Ferretti, C. Prati, and F. Rocca, "Nonlinear subsidence rate estimation using permanent scatterers in differential SAR interferometry," *IEEE Trans. Geosci. Remote Sens.*, vol. 38, no. 5, pp. 2202–2212, Sep. 2000.
[3] P. Berardino, G. Fornaro, R. Lanari, and E. Sansosti, "A new algorithm for surface deformation monitoring based on small baseline differential SAR interferograms," *IEEE Trans. Geosci. Remote Sens.*, vol. 40, no. 11, pp. 2375–2383, Nov. 2002.
[4] A. Hooper, H. Zebker, P. Segall, and B. Kampes, "A new method for measuring deformation on volcanoes and other natural terrains using InSAR persistent scatterers," *Geophyiscal Res. Lett.*, vol. 31, pp. 1–5 2004.
[5] M. Crosetto et al., "The evolution of wide-area DInSAR: From regional and national services to the European ground motion service," *Remote Sens.*, vol. 12, no. 12, 2020, Art. no. 2043.
[6] M. Costantini et al., "European ground motion service (EGMS)," in *Proc. IEEE Int. Geosci. Remote Sens. Symp. IGARSS*, 2021, pp. 3293–3296.
[7] V. D. Navarro-Sanchez, J. M. Lopez-Sanchez, and F. Vicente-Guijalba, "A contribution of polarimetry to satellite differential SAR interferometry: Increasing the number of pixel candidates," *IEEE Geosci. Remote Sens. Lett.*, vol. 7, no. 2, pp. 276–280, Apr. 2010.
[8] V. D. Navarro-Sanchez and J. M. Lopez-Sanchez, "Improvement of persistent-scatterer interferometry performance by means of a polarimetric optimization," *IEEE Geosci. Remote Sens. Lett.*, vol. 9, no. 4, pp. 609–613, Jul. 2012.
[9] Z. Sadeghi, M. J. Valadan Zoej, A. Hooper, and J. M. Lopez-Sanchez, "A new polarimetric persistent scatterer interferometry method using temporal coherence optimization," *IEEE Trans. Geosci. Remote Sens.*, vol. 56, no. 11, pp. 6547–6555, Nov. 2018.
[10] M. Esmaeili and M. Motagh, "Improved persistent scatterer analysis using amplitude dispersion index optimization of dual polarimetry data," *ISPRS J. Photogrammetry Remote Sens.*, vol. 117, pp. 108–114, 2016.
[11] M. Esmaeili, M. Motagh, and A. Hooper, "Application of dual-polarimetry SAR images in multitemporal InSAR processing," *IEEE Geosci. Remote Sens. Lett.*, vol. 14, no. 9, pp. 1489–1493, Sep. 2017.
[12] S. Azadnejad, Y. Maghsoudi, and D. Perissin, "Evaluation of polarimetric capabilities of dual polarized Sentinel-1 and TerraSAR-X data to improve the PSInSAR algorithm using amplitude dispersion index optimization," *Int. J. Appl. Earth Observation Geoinformation*, vol. 84, 2020, Art. no. 101950.
[13] F. Zhao and J. J. Mallorqui, "SMF-POLOPT: An adaptive multitemporal Pol(DIn)SAR filtering and phase optimization algorithm for PSI applications," *IEEE Trans. Geosci. Remote Sens.*, vol. 57, no. 9, pp. 7135–7147, Sep. 2019.
[14] A. G. Mullissa, V. Tolpekin, A. Stein, and D. Perissin, "Polarimetric differential SAR interferometry in an arid natural environment," *Int. J. Appl. Earth Observation Geoinformation*, vol. 59, pp. 9–18, 2017.
[15] V. D. Navarro-Sanchez, J. M. Lopez-Sanchez, and L. Ferro-Famil, "Polarimetric approaches for persistent scatterers interferometry," *IEEE Trans. Geosci. Remote Sens.*, vol. 52, no. 3, pp. 1667–1676, Mar. 2014.
[16] V. D. Navarro-Sanchez and J. M. Lopez-Sanchez, "Spatial adaptive speckle filtering driven by temporal polarimetric statistics and its application to PSI," *IEEE Trans. Geosci. Remote Sens.*, vol. 52, no. 8, pp. 4548–4557, Aug. 2014.
[17] R. Iglesias, D. Monells, X. Fabregas, J. J. Mallorqui, A. Aguasca, and C. Lopez-Martinez, "Phase quality optimization in polarimetric differential SAR interferometry," *IEEE Trans. Geosci. Remote Sens.*, vol. 52, no. 5, pp. 2875–2888, May 2014.

[18] B. Wu, L. Tong, Y. Chen, and L. He, "New methods in multibaseline polarimetric SAR interferometry coherence optimization," *IEEE Geosci. Remote Sens. Lett.*, vol. 12, no. 10, pp. 2016–2020, Oct. 2015.
[19] B. Wu, L. Tong, Y. Chen, and L. He, "Improved SNR optimum method in POLDINSAR coherence optimization," *IEEE Geosci. Remote Sens. Lett.*, vol. 13, no. 7, pp. 982–986, Jul. 2016.
[20] S. Azadnejad, Y. Maghsoudi, and D. Perissin, "Investigating the effect of the physical scattering mechanism of the dual-polarization Sentinel-1 data on the temporal coherence optimization results," *Int. J. Remote Sens.*, vol. 40, no. 18, pp. 7033–7047, 2019.
[21] R. Shamshiri, H. Nahavandchi, and M. Motagh, "Persistent scatterer analysis using dual-polarization Sentinel-1 data: Contribution from VH channel," *IEEE J. Sel. Topics Appl. Earth Observ. Remote Sens.*, vol. 11, no. 9, pp. 3105–3112, Sep. 2018.
[22] F. Zhao et al., "Polarimetric persistent scatterer interferometry for ground deformation monitoring with VV-VH Sentinel-1 data," *Remote Sens.*, vol. 14, no. 2, 2022, Art. no. 309.
[23] A. Hooper, P. Segall, and H. Zebker, "Persistent scatterer interferometric synthetic aperture radar for crustal deformation analysis, with application to Volcan Alcedo, Galapagos," *J. Geophys. Res.*, vol. 112, 2007, Art. no. B07407, doi: 10.1029/2006JB004763.
[24] S. Cloude and K. Papathanassiou, "Polarimetric SAR interferometry," *IEEE Trans. Geosci. Remote Sens.*, vol. 36, no. 5, pp. 1551–1565, Sep. 1998.
[25] M. Neumann, L. Ferro-Famil, and A. Reigber, "Multibaseline polarimetric SAR interferometry coherence optimization," *IEEE Geosci. Remote Sens. Lett.*, vol. 5, no. 1, pp. 93–97, Jan. 2008.
[26] L. Pipia et al., "Polarimetric differential SAR interferometry: First results with ground-based measurements," *IEEE Geosci. Remote Sens. Lett.*, vol. 6, no. 1, pp. 167–171, Jan. 2009.
[27] O. Mora, J. Mallorqui, and A. Broquetas, "Linear and nonlinear terrain deformation maps from a reduced set of interferometric SAR images," *IEEE Trans. Geosci. Remote Sens.*, vol. 41, no. 10, pp. 2243–2253, Oct. 2003.
[28] P. Blanco-Sanchez, J. Mallorqui, S. Duque, and D. Monells, "The coherent pixels technique (CPT): An advanced DInSAR technique for nonlinear deformation monitoring," *Pure Appl. Geophys.*, vol. 165, pp. 1167–1193, 2009.
[29] F. Zhao, J. J. Mallorqui, and J. M. Lopez-Sanchez, "Impact of SAR image resolution on polarimetric persistent scatterer interferometry with amplitude dispersion optimization," *IEEE Trans. Geosci. Remote Sens.*, vol. 60, 2022, Art. no. 5202810.
[30] J. L. Pastor et al., "Multi-source data integration to investigate a deep-seated landslide affecting a bridge," *Remote Sens.*, vol. 11, no. 16, 2019, Art. no. 1878.
[31] J. Delgado et al., "Evaluación de la susceptibilidad de las laderas a sufrir inestabilidades inducidas por terremotos: Aplicación a la cuenca de drenaje del río serpis (provincia de alicante)," *Revista de la Sociedad Geológica de España*, vol. 19, pp. 197–218, 2006.
[32] "Mapa geotécnico y de riesgos geológicos para la ordenación urbana de Alcoy. Mapa de riesgos geológicos E:1/25.000, 1/2.500 y 1/1.000. Memoria," *Ministerio de Industria y Energia*, vol. 3, 1985.
[33] R. Tomas et al., "Mapping ground subsidence induced by aquifer overexploitation using advanced differential SAR interferometry: Vega media of the segura river (SE Spain) case study," *Remote Sens. Environ.*, vol. 98, no. 2, pp. 269–283, 2005.
[34] G. Herrera et al., "Analysis of subsidence using TerraSAR-X data: Murcia case study," *Eng. Geol.*, vol. 116, no. 3-4, pp. 284–295, 2010.
[35] L. Mascolo, S. R. Cloude, and J. M. Lopez-Sanchez, "Model-based decomposition of dual-pol SAR data: Application to Sentinel-1," *IEEE Trans. Geosci. Remote Sens.*, vol. 60, pp. 1–19, 2022.
[36] L. Pipia, X. Fabregas, A. Aguasca, and C. Lopez-Martinez, "Polarimetric temporal analysis of urban environments with a ground-based SAR," *IEEE Trans. Geosci. Remote Sens.*, vol. 51, no. 4, pp. 2343–2360, Apr. 2013.
[37] J. Hu, X.-L. Ding, Z.-W. Li, J.-J. Zhu, Q. Sun, and L. Zhang, "Kalman-filter-based approach for multisensor, multitrack, and multitemporal insar," *IEEE Trans. Geosci. Remote Sens.*, vol. 51, no. 7, pp. 4226–4239, Jul. 2013.
[38] W. An, Y. Cui, and J. Yang, "Three-component model-based decomposition for polarimetric SAR data," *IEEE Trans. Geosci. Remote Sens.*, vol. 48, no. 6, pp. 2732–2739, Jun. 2010.
[39] J.-S. Lee and T. L. Ainsworth, "The effect of orientation angle compensation on coherency matrix and polarimetric target decompositions," *IEEE Trans. Geosci. Remote Sens.*, vol. 49, no. 1, pp. 53–64, Jan. 2011.

Luo Jiayin received the B.S. degree in geomatics engineering from Northeastern University, Shenyang, China, in 2018, and the M.S. degree in geomatics engineering from the State Key Laboratory of Information Engineering in Surveying, Mapping and Remote Sensing, Wuhan University, China, in 2020. She is currently working toward the Ph.D. degree in computer science with the University of Alicante, Alicante, Spain.

Her research interests include polarimetric and interferometric techniques.

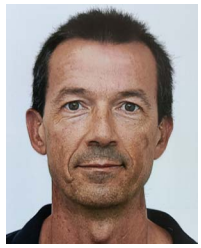

Juan M. Lopez-Sanchez (Senior Member, IEEE) was born in Alicante, Spain, in 1972. He received the Ingeniero (M.S). and Doctor Ingeniero (Ph.D.) degrees in telecommunication engineering from the Technical University of Valencia, Valencia, Spain, in 1996 and 2000, respectively.

From 1998 to 1999, he worked as a Predoctoral Grantholder with the Space Applications Institute, Joint Research Centre of the European Commission, Ispra, Italy. Since 2000, he leads the Signals, Systems and Telecommunication Group of the University of Alicante, Spain, where he has been a Full Professor, since November 2011. He has coauthored more than 100 papers in refereed journals and more than 140 papers and presentations in international conferences and symposia. His research interests include microwave remote sensing for inversion of biophysical parameters, polarimetric and interferometric techniques, and applications of radar remote sensing in agriculture and geophysics.

Dr. Lopez-Sanchez was the recipient of the Indra Award for the best Ph.D. thesis about radar in Spain, in 2001. From 2006 to 2012, he was the Chair of the Spanish Chapter of the IEEE Geoscience and Remote Sensing Society.

Francesco De Zan received the degree in telecommunications engineering, with a focus on signal processing and remote sensing, and the Ph.D. degree in synthetic aperture radar (SAR) interferometry with distributed and decorrelating targets, from Politecnico di Milano, Milan, Italy, from 1998 and 2008, respectively .

He has contributed to the development of the TOPS acquisition mode. In 2007, he visited for two quarters the Stanford Exploration Group, Stanford University, Stanford, CA, USA, which is specialized in the use of seismic waves to image the interior of the Earth. After the conclusion of his Ph.D., he moved to the Munich area (Germany) to join the German Aerospace Center, Cologne, Germany, first with the Microwave and Radar Institute, then with the Remote Sensing Technology Institute. He has worked on aspects related to acquisition planning, performance models for deformation retrieval with InSAR and SAR tomographic applications, orbit design, the calibration of the TanDEM-X interferometer. He has worked on several projects for ESA related to mission design, commissioning and application development for SAR satellites. He has coauthored a few patents in the field of SAR. He has given several introductory lessons at university level on SAR and SAR Interferometry and has supervised some master and Ph.D. theses. His research interests include SAR include performance of phase and delay estimators, ionospheric propagation estimation, focusing and precise geolocation of targets, vegetation and soil moisture effects, inconsistencies in SAR interferometric phases.

Jordi J. Mallorqui Franquet (Senior Member, IEEE) was born in Tarragona, Spain, in 1966. He received the Ingeniero and Doctor Ingeniero degrees in telecommunications engineering from the Universitat Politcnica de Catalunya (UPC), Barcelona, Spain, in 1990 and 1995, respectively.

Since 1993, he has been an Assistant Professor with the School of Telecommunications Engineering of Barcelona, UPC, where he became an Associate Professor, in 1997, and has been a Full Professor, since 2011. From November 2018 to December 2021, he has been the Head of the Signal Theory and Communications Department, UPC. His teaching activity involves microwaves, radio navigation systems, and remote sensing. He spent a sabbatical year with Jet Propulsion Laboratory, Pasadena, CA, USA, in 1999, where he was involved with interferometric airborne synthetic aperture radar (SAR) calibration algorithms. He has authored or coauthored more than 120 papers on microwave tomography, EM numerical simulation, and SAR processing, interferometry, and differential interferometry in refereed journals and international symposia. His research interests include the application of SAR interferometry to terrain-deformation monitoring with orbital, airborne/UAV, and ground-based sensors, vessel detection and classification from SAR images, and 3-D electromagnetic simulation of SAR systems.

Roberto Tomás received the Tech. Eng. (B.S.) degree in civil engineering, the M.S. degree in civil engineering, the M.S. degree in geological engineering, and the Ph.D. degrees in earth sciences and geological engineering from the University of Alicante (UA), Alicante, Spain, in 1998, 2002, 2007, and 2009, respectively.

He is currently a Full Professor of Geotechnical Engineering with the Department of Civil Engineering in the UA. He is Director of the Geotechnical and Structural Engineering research group of the UA, Member of the UNESCO Land Subsidence International Initiative, Coordinator of the Spanish Working Group on land subsidence, and Vicepresident of the Spanish Society for Rock Mechanics. He has led or been involved in more than 50 national and international research projects, as well as over 60 research contracts with companies. He has authored more than 130 scientific articles and more than 230 proceedings, books and book chapters. His research interests include the application of remote sensing techniques for monitoring and modeling of natural hazards (with emphasis in landslides and land subsidence) and infrastructures, as well as for rock mass characterization.